High-Resolution Valley Spectroscopy of Si Quantum Dots

X. Mi,[1] Csaba G. Péterfalvi,[2] Guido Burkard,[2] and J. R. Petta[1]

[1]*Department of Physics, Princeton University, Princeton, New Jersey 08544, USA*
[2]*Department of Physics, University of Konstanz, D-78464 Konstanz, Germany*
(Received 21 April 2017; revised manuscript received 19 August 2017; published 24 October 2017)

We study an accumulation mode Si/SiGe double quantum dot (DQD) containing a single electron that is dipole coupled to microwave photons in a superconducting cavity. Measurements of the cavity transmission reveal dispersive features due to the DQD valley states in Si. The occupation of the valley states can be increased by raising the temperature or applying a finite source-drain bias across the DQD, resulting in an increased signal. Using the cavity input-output theory and a four-level model of the DQD, it is possible to efficiently extract valley splittings and the inter- and intravalley tunnel couplings.

Spin states of electrons in gate-defined semiconductor quantum dots (QDs) are among the leading qubit candidates in efforts to build a solid state quantum processor [1]. Since spin qubits are often indirectly manipulated through electrical means to achieve fast control [2,3], a precise knowledge of the other quantum degrees of freedom (d.o.f.) governing QD electrons is of critical importance for improving the quantum gate fidelities. In III–V semiconductors such as GaAs, these relevant quantum d.o.f. include charge and orbital states, which are reproducibly defined by QD lithographic dimensions and may be spectroscopically probed through a variety of techniques, such as photon-assisted tunneling and pulsed-gate spectroscopy [4,5].

In silicon, which supports long spin lifetimes and is therefore highly suited for spin qubit implementations [6–8], electrons possess an additional quantum d.o.f. The conduction band of bulk Si has six degenerate minima (termed valleys) [9]. In Si/SiGe heterostructures, the four in-plane valleys are raised in energy compared to the two out-of-plane valleys through the strain in the Si quantum well [10,11]. The relatively small energy splitting between the two low-lying valley states has been observed to contribute to spin relaxation [12,13] but may potentially also be harnessed to make charge-noise-insensitive qubits [14]. This valley splitting has been found to vary substantially within the range of 35–270 μeV in Si/SiGe QD devices [15,16], posing an urgent challenge to the reproducibility and scalability of spin qubits based on Si/SiGe heterostructures. A first step toward controlling valley splitting is the development of an experimental method to accurately and efficiently determine its value.

In this Letter, we demonstrate cavity-based spectroscopy of valley states in Si/SiGe double quantum dots (DQDs) using a hybrid circuit quantum electrodynamics (cQED) device architecture [17,18]. Charge transitions involving excited valley states generate observable "fingerprints" in the stability diagram of a cavity-coupled Si/SiGe DQD, as predicted by a recent theory [19]. The occupation of the

valley states can be increased by raising the device temperature or by applying a finite source-drain bias V_{SD} across the DQD. Such a cavity-based valley detection scheme is highly efficient, since it eliminates the need for a magnetic field. Our approach yields information on the valley splitting and intra- and intervalley tunnel couplings and is therefore an attractive alternative to conventional magnetospectroscopy and photon-assisted tunneling [19,20].

The hybrid Si/SiGe cQED device is shown in Fig. 1(a). The cavity is a half-wavelength ($\lambda/2$) Nb transmission line resonator with a center frequency $f_c = 7.796$ GHz, loaded quality factor $Q_c = 2480$, and photon loss rate $\kappa/2\pi = 3.1$ MHz. A DQD is defined in a Si quantum well near a voltage antinode of the cavity [Fig. 1(c)]. Three
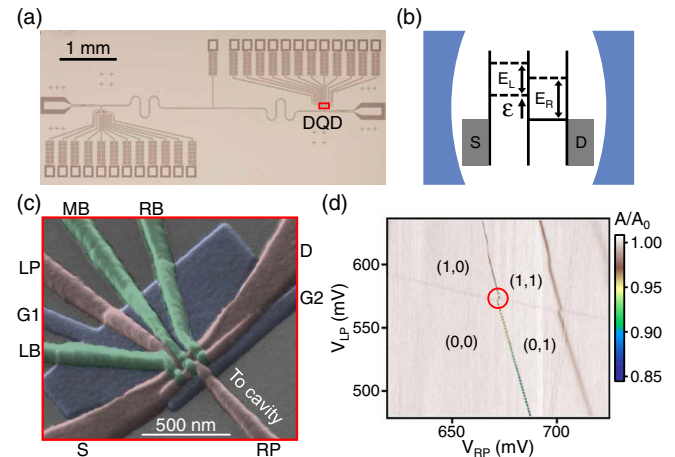

FIG. 1.   (a) Optical image of the device. (b) Schematic representation of the experiment and the DQD energy levels. E_L and E_R denote the valley splittings in the left and right dots, respectively, and ϵ is the interdot level detuning. (c) Tilted angle false-colored scanning electron microscope image of the DQD [red outline in (a)]. (d) DQD charge stability diagram acquired by measuring the cavity transmission amplitude A/A_0 as a function of the plunger gate voltages V_{LP} and V_{RP}, with fixed interdot barrier gate voltage $V_{MB} = 150$ mV.

overlapping layers of Al gates are patterned on top of an undoped Si/SiGe heterostructure to achieve tight electronic confinement (see Ref. [17] for device details). The Si/SiGe heterostructure consists of a 4-nm-thick Si cap, a 50-nm-thick $Si_{0.7}Ge_{0.3}$ spacer layer, an 8-nm-thick Si quantum well, and a 225-nm-thick $Si_{0.7}Ge_{0.3}$ layer grown on top of a $Si_{1-x}Ge_x$ relaxed buffer substrate.

Figure 1(b) shows a schematic representation of the equilibrium configuration of the DQD energy levels. In contrast with previous III/V semiconductor DQD-cQED devices, where two charge states interact with the cavity photons, a total of four charge states are involved in the charge-cavity interaction in this work due to the presence of valley states in Si [21,22]. Electric dipole coupling between DQD electrons and cavity photons is maximized by connecting the gate labeled RP in Fig. 1(c) to the cavity center pin [17,21].

Readout of the DQD charge states is performed in a dilution refrigerator (with base lattice temperature $T_{lat} = 10$ mK) by driving the cavity with a coherent microwave tone at frequency $f = f_c$ and power $P_{in} \approx -128$ dBm (the average intracavity photon number $n_c \approx 1$). A small probe power is chosen so as to not perturb the DQD energy levels from thermal equilibrium. The cavity output field is amplified and demodulated to yield the normalized transmission amplitude A/A_0 and phase $\Delta\phi$ response [17,22,23]. Figure 1(d) shows A/A_0 as a function of plunger gate voltages V_{LP} and V_{RP}, revealing a few-electron DQD charge stability diagram [17,21]. Charge stability islands are labeled with (N_L, N_R), with N_L and N_R being the total number of electrons in the left dot and the right dot, respectively.

We now focus on the $(1,0) \leftrightarrow (0,1)$ interdot charge transition. Figure 2(a) shows A/A_0 as a function of V_{LP} and V_{RP}, with $V_{MB} = 323$ mV. A clear reduction in A/A_0, to a minimum value of ~0.8 (green arrows), is seen along the interdot charge transition where $\epsilon = 0$. Parallel to this central minimum, two additional minima in A/A_0 are also visible (red and blue arrows). The observed cavity response is strikingly different from previously reported devices, where A/A_0 exhibited either a single minimum at $\epsilon = 0$ for $2t_c/h > f_c$ or two minima with similar depths at values of ϵ where $\sqrt{\epsilon^2 + 4t_c^2}/h = f_c$ when $2t_c/h < f_c$ [18,21,22,26,27]. Here t_c is the interdot tunnel coupling. These additional features suggest the presence of higher-lying avoided crossings in the DQD energy level diagram that lead to a nonzero electric susceptibility at finite values of ϵ.

A qualitative understanding of the data can be obtained considering the full DQD energy diagram shown in Fig. 2(b) [19]. Here the DQD is modeled as a four-level system consisting of the left dot ground state $|L\rangle = |(1,0)\rangle$, left dot excited state $|L'\rangle = |(1',0)\rangle$, right dot ground state $|R\rangle = |(0,1)\rangle$, and right dot excited state $|R'\rangle = |(0,1')\rangle$. For large detuning $|\epsilon| > 100$ μeV, valley states within the same dot are separated by the respective valley splitting, E_L
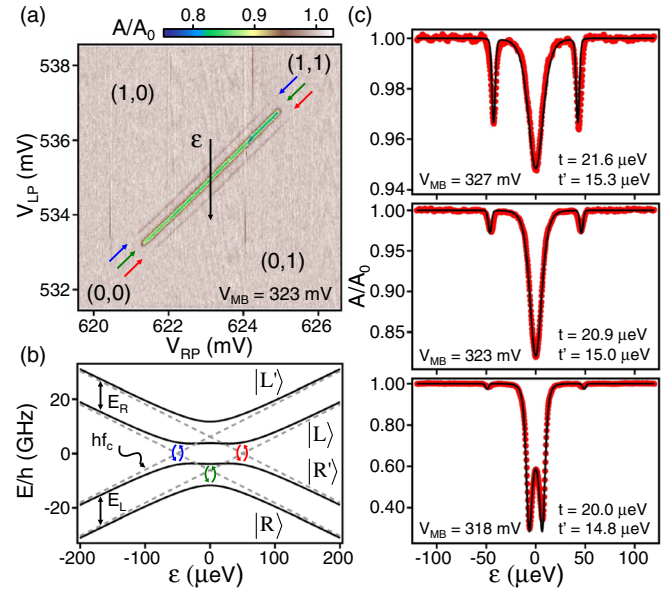

FIG. 2. (a) Cavity transmission amplitude A/A_0 plotted as a function of V_{LP} and V_{RP} near the $(1,0) \leftrightarrow (0,1)$ interdot charge transition with $T_{lat} = 10$ mK. The black arrow denotes the detuning parameter ϵ. (b) DQD energy level diagram with $E_L = E_R = 51$ μeV, $t = 20.9$ μeV, and $t' = 15.0$ μeV. The gray dashed lines show the uncoupled energy levels ($t = t' = 0$). (c) A/A_0 measured as a function of ϵ for three values of V_{MB} and fits to the theory (black lines).

and E_R. For small detuning $|\epsilon| < 100$ μeV, the four states are hybridized by the intravalley tunnel coupling t (t is equivalent to the interdot tunnel coupling t_c in single-valley systems, such as InAs) and the intervalley tunnel coupling t', giving rise to a total of four avoided crossings [19]. The strong minimum in A/A_0 at $\epsilon = 0$ is predominantly due to the avoided crossing involving the DQD ground states $|L\rangle$ and $|R\rangle$ (green arrows), similar to previous work [17,18,21,22,26,27]. The two minima in A/A_0 at $\epsilon \neq 0$ are due to the avoided crossings involving states $|L\rangle$—$|R'\rangle$ (red arrows) and $|L'\rangle$—$|R\rangle$ (blue arrows), located at $\epsilon \approx \pm 50$ μeV. The lower visibility of these two minima arises from the smaller thermal population of the excited states. The $|L'\rangle$—$|R'\rangle$ avoided crossing is expected to have no appreciable contribution to the cavity response due to the negligible population of the two highest-lying states. Moreover, for $E_L \approx E_R$, the $|L'\rangle$—$|R'\rangle$ avoided crossing occurs near $\epsilon = 0$, and its response would be masked by the $|L\rangle$—$|R\rangle$ avoided crossing. The temperature dependence of A/A_0 will be examined in more detail in Fig. 3.

A more quantitative data set is obtained by measuring A/A_0 as a function of ϵ for several values of V_{MB}, which primarily tunes t and t' [Fig. 2(c)]. With $V_{MB} = 327$ mV, the "side minima" have depths comparable to the central minimum at $\epsilon = 0$. When V_{MB} is lowered to 323 mV, the central minimum becomes deeper, whereas the side minima remain relatively unchanged. As V_{MB} is further lowered to 318 mV, the central minimum is split into two minima due to
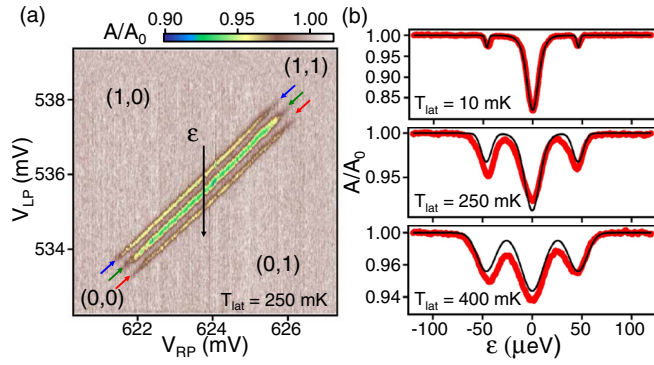
FIG. 3.   (a) A/A_0 plotted as a function of V_{LP} and V_{RP} with $V_{MB} = 323$ mV and $T_{lat} = 250$ mK. (b) A/A_0 as a function of ϵ for three values of T_{lat}, with $V_{MB} = 323$ mV. Black solid lines are theory predictions. The data and fit for $T_{lat} = 10$ mK [Fig. 2(c)] are reproduced here for a direct comparison.

the fact that the $|L\rangle$—$|R\rangle$ transition frequency is now equal to f_c at both $\epsilon = 7\,\mu$eV and $\epsilon = -7\,\mu$eV [18,21,22,27].

The theory developed in Ref. [19] is used to analyze these data. Starting from the four-level system shown in Fig. 2(b), the electric susceptibility χ is calculated as a function of ϵ and used to predict the cavity response A/A_0 with the cavity input-output theory [22]. We simultaneously fit the three data sets shown in Fig. 2(c) to the theory, assuming that changes in V_{MB} modify t and t' but leave E_L and E_R unchanged [19]. The fits to the data are plotted as black lines in Fig. 2(c) and are in excellent agreement with the experimental data with best fit valley splittings $E_L = E_R = 51 \pm 3\,\mu$eV, similar to values found in previous devices [16]. The uncertainties for the valley splittings, estimated based on the linewidths of the side minima, are significantly smaller than those found through magnetospectroscopy, which are typically on the order of 10 μeV [15,16]. The equal valley splitting of the DQD is intentionally achieved through device tuning, and data showing $E_L \neq E_R$ are included in the Supplemental Material [23]. Best fit values of t and t' are listed in Fig. 2(c), which both decrease at lower V_{MB} and show an approximately constant ratio of $t/t' = 1.4$ [19]. Other inputs to the theory are the charge-cavity coupling rate $g_0/2\pi = 19$ MHz, total charge decoherence rate $\gamma/2\pi = 30$ MHz, and electron temperature $T_e = 135$ mK (at the cryostat base temperature $T_{lat} = 10$ mK). Low-frequency charge noise is accounted for in the model by smoothing A/A_0 using a Gaussian with standard deviation $\sigma_\epsilon = 1.5\,\mu$eV [22]. Fits to the cavity phase response (not shown) yield similar results. We also note that the excited states observed here are unlikely to be orbital excited states (orbital energies are around 3 meV in these devices [16]) or spin states due to the single electron occupancy of the DQD and zero external magnetic field.

Since only occupied electronic states will contribute to the electric susceptibility χ, the visibility of the valley-induced features is likely limited by the relatively low electron temperature $k_B T_e \ll E_L \approx E_R$, where k_B is

Boltzmann's constant [19]. This visibility may therefore be improved by raising the temperature of the DQD. Figure 3(a) shows the DQD stability diagram taken at $T_{lat} = 250$ mK. In comparison with Fig. 2(a), the side minima (red and blue arrows) are notably more visible relative to the central minimum. All three minima are also broader. These observations are expected, since, by raising the temperature, the thermal population of the DQD excited states is increased and the ground state population is decreased. This leads to a smaller χ for the $|L\rangle$—$|R\rangle$ avoided crossing but a larger χ for the $|L'\rangle$—$|R\rangle$ and $|L\rangle$—$|R'\rangle$ avoided crossings [19,28]. As a result, the difference between the depths of the side minima and the central minimum in A/A_0 is reduced. On the other hand, background charge noise is also expected to increase at higher temperatures, leading to a broadening of the observed features [29].

Close agreement between the theory and experiment is demonstrated by the plots in Fig. 3(b), where we show A/A_0 as a function of ϵ for $T_{lat} = 10$, 250, and 400 mK. The temperature dependence of the cavity response is theoretically modeled by taking into account the Fermi-Dirac distribution of the electrons in the leads and the Bose-Einstein distribution of the phonon bath, which are assumed to be in equilibrium with the base temperature of the cryostat T_{lat}, except for $T_{lat} = 10$ mK, where the best fit is found with an electron temperature $T_e = 135$ mK. The temperature-dependent charge noise used in the model is $\sigma_\epsilon = 1.5\,\mu$eV for $T_{lat} = 10$ mK, $\sigma_\epsilon = 5\,\mu$eV for $T_{lat} = 250$ mK, and $\sigma_\epsilon = 9\,\mu$eV for $T_{lat} = 400$ mK [29]. The charge decoherence rate $\gamma/2\pi$ has little impact on the theoretical predictions in Fig. 3(b) and is fixed at 30 MHz. In comparison with the data at $T_{lat} = 10$ mK, we conclude that raising the device temperature is an effective method for improving the visibility of the side minima associated with excited valley states.

To improve the visibility of the valley states without increasing the temperature, we may repopulate the valley states via a finite source-drain bias V_{SD}. The lower inset in Fig. 4(a) shows the current through the DQD, I, as a function of V_{LP} and V_{RP} with $V_{SD} = 0.3$ mV. These data exhibit characteristic finite bias triangles (FBTs), as expected for charge transport in a DQD [30]. The main panel in Fig. 4(a) shows A/A_0 measured over the same range of gate voltages, which varies appreciably along the directions defined by the blue, green, and red arrows. In the region between the FBTs, sequential single-electron transport is forbidden due to Coulomb blockade. Here A/A_0 as a function of ϵ is little changed from the $V_{SD} = 0$ data [see Fig. 2(a)]. Within each FBT, electronic transport leads to nonequilibrium populations of the DQD electronic states, and A/A_0 is strongly altered [27]. To give a specific example, we observe an enhancement of the absolute visibility of the $|L'\rangle$—$|R\rangle$ avoided crossing (blue arrow) in the lower FBT [Fig. 4(a)].
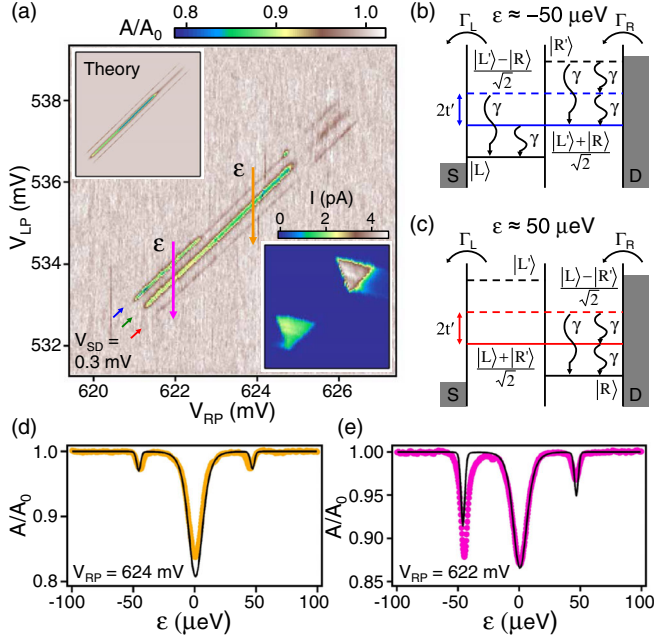
FIG. 4. (a) A/A_0 measured with $V_{MB} = 323$ mV and $V_{SD} = 0.3$ mV. Upper inset: Theory. Lower inset: Measured DQD current I. (b),(c) DQD energy level diagrams at $V_{RP} = 622$ mV for (b) $\epsilon \approx -50$ μeV and (c) $\epsilon \approx 50$ μeV. (d),(e) A/A_0 measured at (d) $V_{RP} = 624$ mV and (e) $V_{RP} = 622$ mV. Black solid lines are fits to the theory.

We can qualitatively understand the nonequilibrium cavity response by considering the transport process within the lower FBT. At $\epsilon \approx -50$ μeV [Fig. 4(b)], the relevant states involved are labeled in the figure, with $(|L'\rangle \pm |R\rangle)/\sqrt{2}$ being hybridized valley-orbit states extended over the two dots. The charge transport cycle starts with the $|0,0\rangle$ state, from which an electron tunnels from the right reservoir at a rate Γ_R into one of the three states available in the right dot. Relaxation processes within the DQD (black curly arrows labeled with rate γ) lead to one of the three states available in the left dot, from which the electron may tunnel with a rate Γ_L onto the left lead. This transport cycle results in an increased population difference between the hybridized valley-orbit states compared to equilibrium and thus a high visibility of the $|L'\rangle$—$|R\rangle$ avoided crossing. In contrast, at the opposite detuning [$\epsilon \approx 50$ μeV; see Fig. 4(c)], an electron may relax into state $|R\rangle$ where it will remain stuck. Consequently, the population difference between the hybridized valley-orbit states $(|L\rangle \pm |R'\rangle)/\sqrt{2}$ is not increased, and no enhancement in the visibility of the $|L\rangle$—$|R'\rangle$ avoided crossing is observed.

To quantitatively model the nonequilibrium cavity response, we solve for the steady state occupation probability ρ_k of each DQD eigenstate $|k\rangle$ (see Supplemental Material for details [23]). Using a Lindblad master equation approach [31], we derive a set of rate equations for ρ_k: $0 = \dot{\rho}_k = \sum_{j \neq k}(\Gamma_{kj}\rho_j - \Gamma_{jk}\rho_k) + \sum_{j \neq k}(\tau_{kj}\rho_j - \tau_{jk}\rho_k)$.

Here $\Gamma_{jk} = \sum_{v=\pm, l=\{L,R\}} \Gamma_l (|\langle j|c_{l,v}|k\rangle|^2 + |\langle k|c_{l,v}|j\rangle|^2) n_{jk}^{(l)}$ denotes the transition rate from state k to state j due to an electron tunneling on or off the DQD, with Γ_l being the tunneling rate to lead l, $c_{l,v}$ the annihilation operator for electrons in dot l and valley v, and the $n_{jk}^{(l)}$ factors account for the finite temperature in the source-drain leads. The sum $\sum_{j \neq k}(\tau_{kj}\rho_j - \tau_{jk}\rho_k)$ describes decay processes between states with the same total number of electrons, where the decay rate $\tau_{jk} \sim \gamma$ for states with one electron in the DQD. The resulting values of ρ_k are then used to calculate A/A_0 via the cavity input-output theory [19].

The experimental data in Figs. 4(d) and 4(e) are fit to the theory, yielding best fit tunneling rates $\Gamma_L = 62$ MHz, $\Gamma_R = 132$ MHz, and $\gamma = 188$ MHz. In the upper inset in Fig. 4(a), we have calculated A/A_0 over the same gate voltage range as the data using these parameters and a capacitance matrix-based model of the DQD [4,23]. The discrepancy between the data and theory at $\epsilon = -50$ μeV may be due to the simplicity of the theoretical model, which takes the same decay rate γ for all transitions and assumes energy-independent tunneling rates Γ_L and Γ_R. We also note that two factors in the DQD tunneling rates facilitate the improved visibility of the $|L'\rangle$—$|R\rangle$ avoided crossing: First, γ is comparable to Γ_L and Γ_R, ensuring the populations of the $|L'\rangle$ and $|R\rangle$ states neither relax to thermal equilibrium due to slow loading or unloading from the leads nor become nearly equal due to fast loading or unloading. Second, the loading rate Γ_R is larger than Γ_L such that the DQD spends negligible time in the empty state $|0\rangle$, which has zero charge susceptibility. Finally, we note that an enhancement in the absolute visibility of the $|L\rangle$—$|R'\rangle$ avoided crossing (red arrows) is seen in the upper FBT with $V_{SD} = -0.3$ mV (see data in Ref. [23]).

In conclusion, we observe dispersive features in the cavity response of a hybrid Si/SiGe DQD-cQED device that arise from the valley d.o.f. in Si. The cavity response is sensitive to the valley splitting in each dot, the inter- and intravalley tunnel couplings, and the time-averaged occupation of the levels [19]. The relative occupation of the DQD energy levels can be driven out of equilibrium by increasing the temperature or applying a source-drain bias, thereby increasing the visibility of the valley states. These measurements constitute an efficient method for accurate spectroscopy of valley states in Si/SiGe heterostructures and are applicable to other Si devices, such as Si metal-oxide-semiconductor quantum dots. Rapid and accurate measurements of the valley splitting may accelerate progress toward understanding, and ultimately controlling, valley splittings in these highly relevant quantum devices.

[1] D. Loss and D. P. DiVincenzo, Phys. Rev. A **57,** 120 (1998).

[2] J. R. Petta, A. C. Johnson, J. M. Taylor, E. A. Laird, A. Yacoby, M. D. Lukin, C. M. Marcus, M. P. Hanson, and A. C. Gossard, Science **309,** 2180 (2005).

[3] B. M. Maune, M. G. Borselli, B. Huang, T. D. Ladd, P. W. Deelman, K. S. Holabird, A. A. Kiselev, I. Alvarado-Rodriguez, R. S. Ross, A. E. Schmitz, M. Sokolich, C. A. Watson, M. F. Gyure, and A. T. Hunter, Nature (London) **481,** 344 (2012).

[4] W. G. van der Wiel, S. De Franceschi, J. M. Elzerman, T. Fujisawa, S. Tarucha, and L. P. Kouwenhoven, Rev. Mod. Phys. **75,** 1 (2002).

[5] J. M. Elzerman, R. Hanson, L. H. Willems van Beveren, B. Witkamp, L. M. K. Vandersypen, and L. P. Kouwenhoven, Nature (London) **430,** 431 (2004).

[6] A. M. Tyryshkin, S. Tojo, J. J. L. Morton, H. Riemann, N. V. Abrosimov, P. Becker, H.-J. Pohl, T. Schenkel, M. L. W. Thewalt, K. M. Itoh, and S. A. Lyon, Nat. Mater. **11,** 143 (2012).

[7] M. Veldhorst, J. C. C. Hwang, C. H. Yang, A. W. Leenstra, B. de Ronde, J. P. Dehollain, J. T. Muhonen, F. E. Hudson, K. M. Itoh, A. Morello, and A. S. Dzurak, Nat. Nanotechnol. **9,** 981 (2014).

[8] D. M. Zajac, T. M. Hazard, X. Mi, E. Nielsen, and J. R. Petta, Phys. Rev. Applied **6,** 054013 (2016).

[9] T. Ando, A. B. Fowler, and F. Stern, Rev. Mod. Phys. **54,** 437 (1982).

[10] F. Schäffler, Semicond. Sci. Technol. **12,** 1515 (1997).

[11] F. A. Zwanenburg, A. S. Dzurak, A. Morello, M. Y. Simmons, L. C. L. Hollenberg, G. Klimeck, S. Rogge, S. N. Coppersmith, and M. A. Eriksson, Rev. Mod. Phys. **85,** 961 (2013).

[12] C. H. Yang, A. Rossi, R. Ruskov, N. S. Lai, F. A. Mohiyaddin, S. Lee, C. Tahan, G. Klimeck, A. Morello, and A. S. Dzurak, Nat. Commun. **4,** 2069 (2013).

[13] E. Kawakami, P. Scarlino, D. R. Ward, F. R. Braakman, D. E. Savage, M. G. Lagally, M. Friesen, S. N. Coppersmith, M. A. Eriksson, and L. M. K. Vandersypen, Nat. Nanotechnol. **9,** 666 (2014).

[14] D. Culcer, A. L. Saraiva, B. Koiller, X. Hu, and S. Das Sarma, Phys. Rev. Lett. **108,** 126804 (2012).

[15] M. G. Borselli, R. S. Ross, A. A. Kiselev, E. T. Croke, K. S. Holabird, P. W. Deelman, L. D. Warren, I. Alvarado-Rodriguez, I. Milosavljevic, F. C. Ku, W. S. Wong, A. E. Schmitz, M. Sokolich, M. F. Gyure, and A. T. Hunter, Appl. Phys. Lett. **98,** 123118 (2011).

[16] D. M. Zajac, T. M. Hazard, X. Mi, K. Wang, and J. R. Petta, Appl. Phys. Lett. **106,** 223507 (2015).

[17] X. Mi, J. V. Cady, D. M. Zajac, J. Stehlik, L. F. Edge, and J. R. Petta, Appl. Phys. Lett. **110,** 043502 (2017).

[18] X. Mi, J. V. Cady, D. M. Zajac, P. W. Deelman, and J. R. Petta, Science **355,** 156 (2017).

[19] G. Burkard and J. R. Petta, Phys. Rev. B **94,** 195305 (2016).

[20] K. Wang, C. Payette, Y. Dovzhenko, P. W. Deelman, and J. R. Petta, Phys. Rev. Lett. **111,** 046801 (2013).

[21] T. Frey, P. J. Leek, M. Beck, A. Blais, T. Ihn, K. Ensslin, and A. Wallraff, Phys. Rev. Lett. **108,** 046807 (2012).

[22] K. D. Petersson, L. W. McFaul, M. D. Schroer, M. Jung, J. M. Taylor, A. A. Houck, and J. R. Petta, Nature (London) **490,** 380 (2012).

[23] See Supplemental Material at http://link.aps.org/supplemental/10.1103/PhysRevLett.119.176803 for data from devices with unequal valley splittings $E_L \neq E_R$, data for A/A_0 at $V_{\mathrm{SD}} = -0.3$ mV, and details of the theory used in modeling the data in Fig. 4. Supplemental Material also contains Refs. [24, 25].

[24] J. K. Gamble, M. A. Eriksson, S. N. Coppersmith, and M. Friesen, Phys. Rev. B **88,** 035310 (2013).

[25] M. J. Collett and C. W. Gardiner, Phys. Rev. A **30,** 1386 (1984).

[26] G.-W. Deng, D. Wei, J. R. Johansson, M.-L. Zhang, S.-X. Li, H.-O. Li, G. Cao, M. Xiao, T. Tu, G.-C. Guo, H.-W. Jiang, F. Nori, and G.-P. Guo, Phys. Rev. Lett. **115,** 126804 (2015).

[27] J. J. Viennot, M. R. Delbecq, M. C. Dartiailh, A. Cottet, and T. Kontos, Phys. Rev. B **89,** 165404 (2014).

[28] M. D. Schroer, M. Jung, K. D. Petersson, and J. R. Petta, Phys. Rev. Lett. **109,** 166804 (2012).

[29] O. E. Dial, M. D. Shulman, S. P. Harvey, H. Bluhm, V. Umansky, and A. Yacoby, Phys. Rev. Lett. **110,** 146804 (2013).

[30] R. Hanson, L. P. Kouwenhoven, J. R. Petta, S. Tarucha, and L. M. K. Vandersypen, Rev. Mod. Phys. **79,** 1217 (2007).

[31] H.-P. Breuer and F. Petruccione, *The Theory of Open Quantum Systems* (Oxford University, New York, 2007).